Fluid modeling of resistive plate chambers: impact of transport data on development of streamers and induced signals

2016 J. Phys. D: Appl. Phys. 49 405201

(http://iopscience.iop.org/0022-3727/49/40/405201)

IOP Publishing Journal of Physics D: Applied Physics
J. Phys. D: Appl. Phys. **49** (2016) 405201 (10pp) doi:10.1088/0022-3727/49/40/405201

Fluid modeling of resistive plate chambers: impact of transport data on development of streamers and induced signals

D Bošnjaković[1], Z Lj Petrović[1,2] and S Dujko[1]

[1] Institute of Physics, University of Belgrade, Pregrevica 118, 11080 Belgrade, Serbia
[2] Serbian Academy of Sciences and Arts, Knez Mihailova 35, 11001 Belgrade, Serbia

E-mail: dbosnjak@ipb.ac.rs

Received 13 May 2016, revised 29 July 2016
Accepted for publication 12 August 2016
Published 9 September 2016

Abstract

We discuss the implementation of transport data in modeling of resistive plate chambers (RPCs), which are used for timing and triggering purposes in many high energy physics experiments. Particularly, we stress the importance of making a distinction between flux and bulk transport data when non-conservative collisions, such as attachment and/or ionization, are present. A 1.5-dimensional fluid model with photoionization is employed to demonstrate how the duality of transport data affects the calculated signals of the ATLAS triggering RPC and ALICE timing RPC used at CERN, and also a timing RPC with high SF_6 content. It is shown that in the case of timing RPCs, the difference between the induced charges calculated using flux and bulk transport data can reach several hundred percent at lower operating electric fields. The effects of photoionization and space charge are also discussed.

Keywords: resistive plate chambers, fluid models, electron avalanche, streamers, photoionization, $C_2H_2F_4$

(Some figures may appear in colour only in the online journal)

1. Introduction

Introduced in the 1980s [1, 2], resistive plate chambers (RPCs) became widely used particle detectors for large area timing and triggering purposes in high energy physics experiments [3–5]. They consist of one or many gas gaps between electrodes of high resistivity such as glass or bakelite. Owing to their low cost, good efficiency and outstanding timing resolution [6, 7], RPCs found their way into other areas of fundamental physics and technology, including cosmic ray physics [8], geophysics [9] and medical imaging [10].

There have been many approaches to modeling of RPCs. Analytical methods [11, 12], while often approximate, can provide general conclusions about the influence of various parameters on the RPC performance. Monte Carlo simulations [13–15] are useful for calculating RPC performance characteristics, such as timing resolution and efficiency, which depend on the stochastic nature of primary ionization and electron avalanche development. On the other hand, numerical models based on fluid equations [16, 17] can only provide the mean values of RPC signals. Still, they are frequently used for studying various physical phenomena in RPC operation, in a computationally efficient manner.

All RPC models, except the microscopic Monte Carlo model [15], rely on accurate electron transport and reaction data in gases [18]. These data can be obtained from swarm experiments [19, 20] but are usually calculated from the electron impact cross sections using either the Monte Carlo technique [21, 22] or Boltzmann equation analysis [23–25]. MAGBOLTZ [26] is a Monte Carlo tool for such a task and is routinely used by the particle detector community. However, there seems to be a lack of awareness of the two types of transport data named ‘flux’ and ‘bulk’ [19, 27]. The difference between the two can be elucidated by the explicit effects of non-conservative collisions. Every collision which results in changing of the number of electrons in the ensemble (e.g. ionization, attachment, electron–ion recombination) is regarded as non-conservative. In RPC

modeling, flux data were assumed systematically. Still, to our knowledge, MAGBOLTZ can compute the bulk data and considers them as 'time of flight' data, in the framework of the so-called 'Tagashira convention' [28]. Furthermore, most swarm experiments measure bulk properties [19, 25] and as of recently, BOLSIG + [29]—a publicly available two term Boltzmann equation solver—can also compute the bulk data. Differences between two sets of data are often significant, ranging from a few percent to a few orders of magnitude. In some cases, bulk and flux transport coefficients may exhibit entirely different qualitative behavior, as in case of negative absolute electron flux mobility [30] in mixtures of noble and strongly attaching gases and negative differential conductivity (NDC) for electron bulk drift velocity in strongly attaching gases [31]. A question may be raised as to which data, under which conditions, are appropriate in modeling of RPCs. The aim of this paper is to discuss this issue and also to demonstrate the difference one might induce by implementation with the bulk and flux data in fluid modeling of RPCs. With that motivation, we have developed a fluid model based on a drift-diffusion equation in a 1.5-dimensional framework. This numerical model is also used to investigate streamer development in RPCs under the influence of space charge effects and photoionization. Particularly, we focus on the signal formation in three RPC configurations with different SF_6 content, where duality of transport data should not be neglected.

In the present paper, we extend the previous fluid-equation based models of RPCs [16, 17] by including the diffusion term in the fluid model. In addition to ATLAS triggering RPC, we present what we believe to be the first systematic calculation of the induced signals in the ALICE timing RPC and timing RPC [32] for a wide range of the applied electric fields. Electron transport coefficients as a function of the reduced electric field are required as input in fluid equations. A Monte Carlo simulation technique is used to calculate these transport coefficients in the gas mixtures considered in this work. In particular, a new set of cross sections for electron scattering in $C_2H_2F_4$ is developed and considered in the calculations.

This paper is organized as follows. In section 2.1 we give a brief overview and theoretical basis of electron transport in gases under the hydrodynamic assumption and highlight those aspects relevant for modeling. The numerical model used to study the signal formation in ATLAS triggering RPC, ALICE timing RPC and timing RPC [32] is described in section 2.3. Calculated transport data used as input in this model are presented in section 2.2. Finally, in section 3 we show how different transport data affect the calculated signals for the three RPC configurations.

2. Theoretical methods

2.1. Hydrodynamic modeling of electron transport in gases

The starting point of our electron transport analysis is the equation of continuity

$$\frac{\partial n_e(\mathbf{r},t)}{\partial t} + \nabla \cdot \mathbf{\Gamma}(\mathbf{r},t) = S(\mathbf{r},t), \tag{1}$$

where $n_e(\mathbf{r},t)$ is the electron number density, $\mathbf{\Gamma}(\mathbf{r},t) = n_e\langle\mathbf{v}\rangle$ is the electron flux, $\langle\mathbf{v}\rangle$ is the average electron velocity and $S(\mathbf{r},t)$ represents the electron production rate per unit volume arising from non-conservative collisions. Away from electrodes, sources and sinks of electrons, the hydrodynamic conditions can be assumed [22, 33]. Under these conditions, the phase-space distribution function can be expressed as

$$f(\mathbf{r},\mathbf{v},t) = \sum_{k=0}^{\infty} f^{(k)}(\mathbf{v}) \odot (-\nabla)^k n_e(\mathbf{r},t), \tag{2}$$

where $f^{(k)}(\mathbf{v})$ are tensors of rank k and $\odot$ denotes a k-scalar product. This functional relationship, which is valid for weak gradients, is known as the hydrodynamic approximation [33]. Using the expansion (2), after truncation, the flux $\mathbf{\Gamma}(\mathbf{r},t)$ and source term $S(\mathbf{r},t)$ in the continuity equation (1) can be written as

$$\mathbf{\Gamma}(\mathbf{r},t) = \mathbf{W}_F n_e(\mathbf{r},t) - \mathbf{D}_F \cdot \nabla n_e(\mathbf{r},t), \tag{3}$$

$$S(\mathbf{r},t) = S^{(0)} n_e(\mathbf{r},t) - \mathbf{S}^{(1)} \cdot \nabla n_e(\mathbf{r},t) + \mathbf{S}^{(2)} : \nabla\nabla n_e(\mathbf{r},t), \tag{4}$$

where $\mathbf{W}_F$ is the flux drift velocity and $\mathbf{D}_F$ is the flux diffusion tensor. Substituting the expressions for the flux (3) and source term (4) into the continuity equation (1) we obtain

$$\frac{\partial n_e(\mathbf{r},t)}{\partial t} + \nabla \cdot (\mathbf{W}_B n_e(\mathbf{r},t) - \mathbf{D}_B \cdot \nabla n_e(\mathbf{r},t)) = S^{(0)} n_e(\mathbf{r},t), \tag{5}$$

where

$$\mathbf{W}_B = \mathbf{W}_F + \mathbf{S}^{(1)} \quad \text{(bulk drift velocity)}, \tag{6}$$

$$\mathbf{D}_B = \mathbf{D}_F + \mathbf{S}^{(2)} \quad \text{(bulk diffusion tensor)}. \tag{7}$$

The equation (5) is strictly valid only when $\nabla\mathbf{S}^{(1)} n_e - \nabla\mathbf{S}^{(2)}\nabla n_e = 0$. This assumption holds when the electric field is spatially homogeneous as in the avalanche phase of streamer development in RPCs. It is possible to avoid this assumption, and this analysis is deferred to a future paper. Our preliminary results, obtained under conditions found in RPCs suggest that equation (5) is valid even for the streamer phase where the space charge effects control the electric field. From definitions (6) and (7), it is evident that the difference between the flux and bulk transport coefficients arises only due to presence of non-conservative collisions. It is shown [33, 34] that the bulk drift velocity can also be defined as

$$\mathbf{W}_B = \frac{\mathrm{d}}{\mathrm{d}t}\langle\mathbf{r}\rangle, \tag{8}$$

and the bulk diffusion tensor as

$$\mathbf{D}_B = \frac{1}{2}\frac{\mathrm{d}}{\mathrm{d}t}\langle\mathbf{r}^*\mathbf{r}^*\rangle. \tag{9}$$

Here $\mathbf{r}^* = \mathbf{r} - \langle\mathbf{r}\rangle$ where $\langle\mathbf{r}\rangle$ is the mean position of the swarm. Similarly, the flux drift velocity components and the flux diagonal elements of the diffusion tensor are defined as

$$\mathbf{W}_F = \left\langle \frac{\mathrm{d}\mathbf{r}}{\mathrm{d}t} \right\rangle = \langle\mathbf{v}\rangle, \tag{10}$$

$$\mathbf{D}_{F,ii} = \langle\mathbf{r}_i\mathbf{v}_i\rangle - \langle\mathbf{r}_i\rangle\langle\mathbf{v}_i\rangle, \tag{11}$$

where $\langle \mathbf{v}_i \rangle$ is the mean electron velocity and $i = x,y,z$. The definitions (8)–(11) are useful for direct sampling in Monte Carlo simulations. Also, the electron production rate $S^{(0)}$ can be calculated as

$$S^{(0)} = \frac{1}{N_e}\frac{dN_e}{dt}, \tag{12}$$

where $N_e(t)$ is the number of electrons in the swarm.

One should be aware of the differences between the bulk drift velocity and flux drift velocity. The bulk drift velocity (8) is the velocity of centre of mass of the swarm, while the flux drift velocity (10) is the mean velocity of electrons. It can be easily illustrated why the two velocities may differ in presence of non-conservative collisions. Even under hydrodynamic conditions, in constant electric field, the mean energy of electrons is not constant throughout the swarm [24, 25, 31]. Electrons at the front of the swarm generally have higher energy than those at the back. If the collision frequency for ionization increases with the electron energy, then electrons are predominantly created in regions of higher energy, resulting in a shift of the centre of mass of the swarm. A similar physical picture can be applied for electron attachment: if there is an attachment process which occurs at higher collision energies, it will naturally tend to affect the leading edge of the swarm. This results in a backwards shift of the swarm's centre of mass, which is observable as a reduction of the bulk drift velocity (as compared to the flux drift velocity). This process is known as attachment cooling [35, 36]. Conversely, if collision frequency for electron attachment decreases with the electron energy, then it is more likely that electrons will be more efficiently consumed at the back than on the leading edge of the swarm. This in turn shifts the swarm's centre of mass forward. This phenomenon is observable as an increase of the bulk drift velocity and is usually known in the literature as attachment heating [35, 36]. The distinction between the two velocity components has important implications in modeling of electron avalanches. One should take into account that the avalanche (i.e. its centre of mass) progresses in space with bulk drift velocity. For example, when Legler's model [37], or any other model of avalanche fluctuations is employed as a function of avalanche path length [14, 38], bulk drift velocity should be used to evaluate the ionization and attachment coefficients.

Transport quantities (8)–(12) can be considered as fundamental data. They are strictly defined under hydrodynamic conditions and are not an artifact of a particular theoretical model or method of analysis. They are measurable and independent of the experimental arrangement. Most swarm experiments involve determination of bulk transport properties. Typical examples are the pulsed-Townsend experiment and time-of-flight experiment [19, 27]. These experiments assume hydrodynamic conditions, which means that the measured quantities correspond to the bulk properties appearing in the diffusion equation (5). The bulk transport properties can be used to normalize the sets of cross sections using the so-called swarm procedure. The normalized set of cross sections for electron scattering provides transport and reaction data which are in a good agreement with the measured data. The standard swarm procedure was used by our group with the aim of deriving the cross sections for electron scattering $C_2H_2F_4$ (section 2.2). As a result of this procedure, the calculated transport coefficients agree very well with those measured under the pulsed-Townsend conditions [39, 40].

Equation (5) coupled with the Poisson equation using a local field approximation forms the basis of the fluid model considered in this work. Local field approximation assumes that the electrons are in equilibrium with the local electric field and thus the properly defined transport coefficients are only functions of the local electric field. The equation (5) also assumes hydrodynamic conditions and the approximation concerning the source term. However, for homogeneous electric field, this model gives the correct avalanche velocity and ionization per avalanche path length. The same might not be true for fluid models of RPCs [16–18] where the type of transport data used as input is not discussed. Equation (5) with flux transport coefficients instead of bulk, forms the basis of the first-order fluid model. The designation 'first-order' implies that it can be derived from the Boltzmann transport equation using first-order velocity moments of the phase-space distribution function and several approximations [41]. In general, fluid models can be derived as moment equations of the variable order but they usually require many simplifying and closure assumptions. For example, the fluid model of the second-order is truncated at the level of the mean energy where fluid equations are closed in the so-called local mean energy approximation [41, 42]. Higher-order models introduce even more equations and have been used for studying the non-local effects in streamer dynamics [41, 42]. The application of high-order fluid models for analysis of RPCs is a subject of our forthcoming paper. In this paper, however, we only consider the first-order model with flux transport data and model based on equation (5) with bulk transport data. Since both models are mathematically the same, with the only difference being the transport data used as input, we shall refer to them as a single model which uses either flux or bulk transport data.

2.2. Electron transport data in RPC gases

In this section we present the calculated transport and rate coefficients for fluid modeling of the three RPC configurations. The data are calculated using our Monte Carlo technique based on tracking of individual electrons and their collisions with the background gas. We assume that the electron scattering is isotropic for each type of collision. While the inclusion of anisotropy of electron scattering is important for modeling of the transport and discharges in some molecules under mostly high energy conditions no such conditions were found in the present work that would justify the need to include the differential cross sections and also that would be supported by the available data to a sufficient degree. The background gas temperature is set to 293 K. The transport coefficients are sampled using definitions (8)–(11). For more details about our Monte Carlo code the reader is referred to [21, 34, 43].

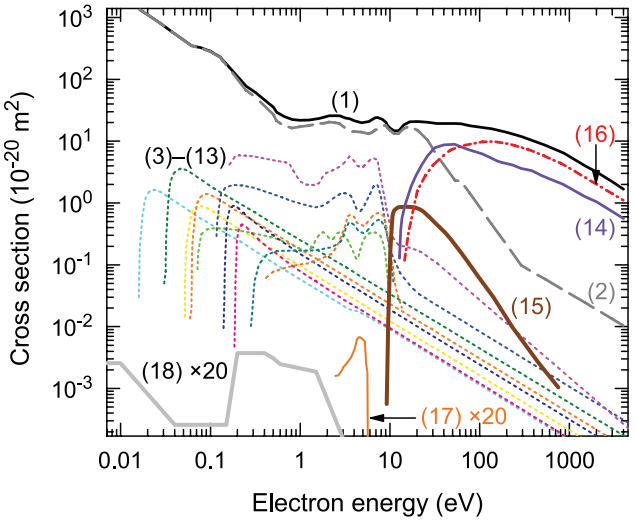

Figure 1. Cross sections for electron scattering in $C_2H_2F_4$ [44]: (1) total momentum transfer, (2) elastic momentum transfer, (3)–(13) vibrational excitations, (14) dissociative excitation, (15) effective electronic excitation, (16) ionization, (17) dissociative attachment, (18) 3-body attachment assuming pressure of 1 atm and temperature of 293 K. For display, the attachment cross sections (17) and (18) are multiplied by factor 20.

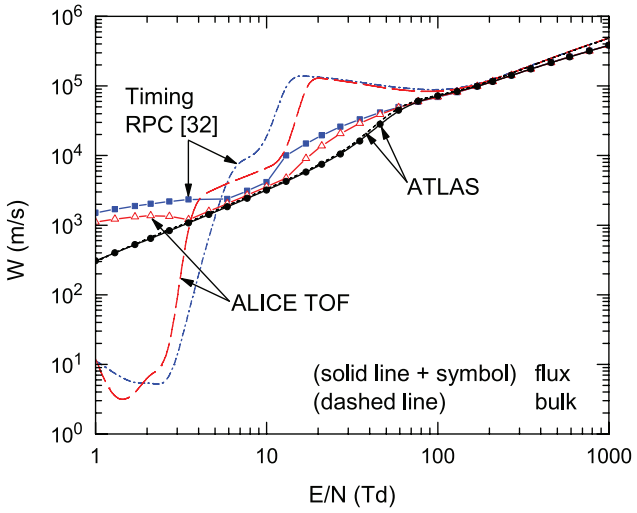

Figure 2. Bulk and flux drift velocities calculated for gas mixtures used in ATLAS triggering RPC, ALICE timing RPC and timing RPC [32].

The transport and rate coefficients are calculated for gas mixtures employed in: (1) ATLAS triggering RPC [3] 94.7% $C_2H_2F_4$ + 5% iso-C_4H_{10} + 0.3% SF_6, (2) ALICE timing RPC [4] 90% $C_2H_2F_4$ + 5% iso-C_4H_{10} + 5% SF_6, and (3) timing RPC [32] 85% $C_2H_2F_4$ + 5% iso-C_4H_{10} + 10% SF_6. The data are calculated using a new cross section set for electron scattering in $C_2H_2F_4$ (figure 1) developed by our group [44]. This cross section set is based on an updated version of our previous set [45] with additional vibrational excitations, electronic excitation and three-body attachment. The transport and rate coefficients obtained using this set are in good agreement with measurements by Urquijo *et al* [40] and Basile *et al* [39]. The cross sections for iso-C_4H_{10} are taken from MAGBOLTZ 7.1. There is an updated set for iso-C_4H_{10} in newer versions of MAGBOLTZ but the ionization coefficient obtained using the older set from MAGBOLTZ 7.1 is in better agreement with measurements [46]. Finally, the cross section set for electron scattering in SF_6 is taken from Itoh *et al* [47].

Figure 2 shows the flux and bulk drift velocities calculated over a range of reduced electric field strengths for three RPC gas mixtures. The reduced electric field E/N is expressed in Td (1 Td = 10^{-21} Vm^2). We observe that the ALICE timing RPC and timing RPC [32] gas mixtures exhibit the greatest overall difference between bulk and flux components of drift velocity. The difference is larger than two orders of magnitude in the limit of the lowest fields considered in this work (1–3 Td) and an order of magnitude between 10–30 Td. In both of these E/N ranges we see that the bulk drift velocity is reduced for an increasing E/N. This phenomenon is termed negative differential conductivity (NDC) and has been studied many times in the past [48, 49]. In particular, the occurrence of NDC in the bulk drift velocity in the ALICE timing RPC gas mixture has already been investigated in [31]. Still, the largest differences between the flux and bulk components are in the attachment dominated region below 100 Td (figure 3). In the ionization dominated region, at RPC operating fields of 200–400 Td, the difference ranges between 5% and 15%. A similar behavior is observed in the longitudinal component of the diffusion tensor (figure 4).

2.3. Numerical model

Assuming one-dimensional scenario $n_e(\mathbf{r}, t) = n_e(x, t)$ and the electric field $\mathbf{E} = E\,\mathbf{e}_x$ (where $\mathbf{e}_x$ is the unit vector in the x direction), with addition of the photoionization source term (S_{ph}), the equation (5) reduces to

$$\frac{\partial n_e}{\partial t} = \frac{\partial}{\partial x}\left(W\,\mathrm{sgn}(E)\,n_e + D_L\,\frac{\partial n_e}{\partial x}\right) + (\nu_i - \nu_a)\,n_e + S_{ph}, \tag{13}$$

where ν_i and ν_a are the ionization and attachment frequencies (figure 3) respectively. The drift velocity W is defined as positive (figure 2) and sgn(E) is the sign (signum) function. Both transport and reaction data are considered as functions of $|E(x, t)|$. The continuity equations for the number densities of positive (n_p) and negative ions (n_n) are written as

$$\frac{\partial n_p}{\partial t} = \nu_i\,n_e + S_{ph} \quad \text{and} \quad \frac{\partial n_n}{\partial t} = \nu_a\,n_e, \tag{14}$$

since the ions can be considered as immobile on the timescale of fast electron signals.

The electric field is calculated assuming that the charge is contained inside a cylinder, with radius R_0 along the x axis, and distributed uniformly in the radial direction. In this case, similar to [50], the electric field along the x axis is given by

$$E(x,t) = E_0 + \frac{e_0}{2\varepsilon_0}\int_0^d (n_p(x',t) - n_n(x',t) - n_e(x',t)) \cdot \left(\mathrm{sgn}\,(x - x') - \frac{x - x'}{\sqrt{(x - x')^2 + R_0^2}}\right) \mathrm{d}x', \tag{15}$$

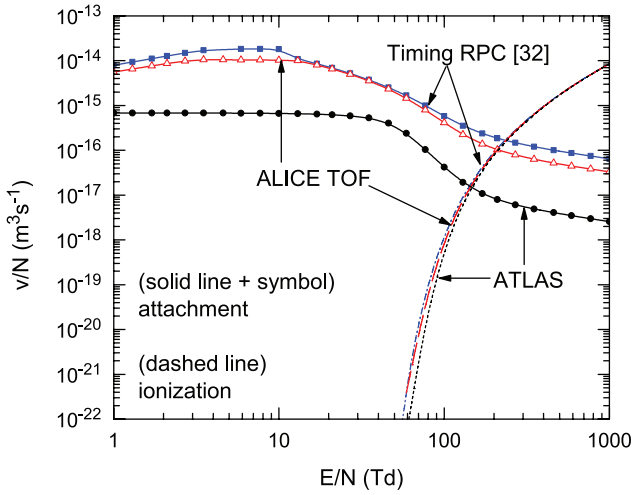

Figure 3. Ionization and attachment rate coefficients calculated for gas mixtures used in ATLAS triggering RPC, ALICE timing RPC and timing RPC [32].

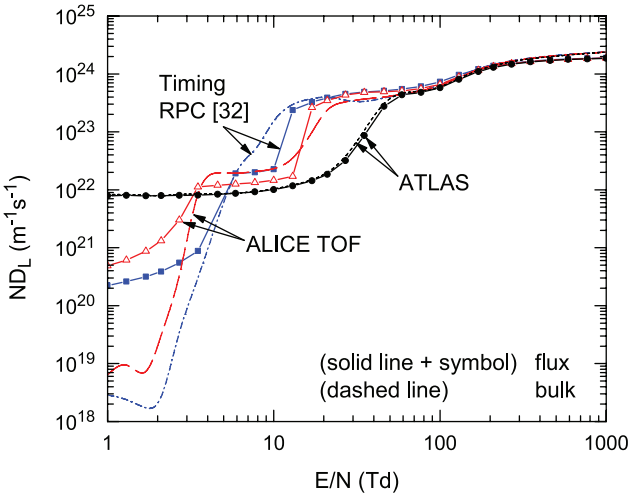

Figure 4. Bulk and flux density-normalized longitudinal diffusion coefficient calculated for gas mixtures used in ATLAS triggering RPC, ALICE timing RPC and timing RPC [32].

where E_0, d, e_0 and ε_0 are the external (applied) electric field, gas gap length, elementary charge and vacuum permittivity respectively.

The photoionization source term is defined as [51, 52]

$$S_{\mathrm{ph}}(x,t) = \frac{M}{2\lambda}\int_0^d \nu_{\mathrm{i}}(|E(x',t)|)\, n_{\mathrm{e}}(x',t)\; \Omega\,(x-x') \cdot \exp\left(-\frac{|x-x'|}{\lambda}\right) \mathrm{d}x', \tag{16}$$

where factor $M \equiv Q\nu_{\mathrm{ph}}/\nu_{\mathrm{i}}$ is the global photoionization efficiency. As an approximation, the model assumes that the photon production frequency ν_{ph} is proportional to the ionization frequency ν_{i}. The photon mean free path λ and the photoionization quantum efficiency Q are considered as effective values, averaged over the relevant photoemission bands. The function

$$\Omega\,(x-x') = \frac{1}{2}\left(1 - \frac{|x-x'|}{\sqrt{(x-x')^2 + R_0^2}}\right), \tag{17}$$

represents fraction of the solid angle centred at the emission point x' and covering the cross section area at x.

Equations (13) and (14) are solved numerically, imposing boundary conditions for absorbing electrodes

$$n_{\mathrm{e}}(x=0,t) = 0, \quad n_{\mathrm{e}}(x=d,t) = 0, \tag{18}$$

and initial conditions

$$n_{\mathrm{e}}(x,t=0) = \frac{N_{\mathrm{e0}}}{\pi R_0^2\,\sigma_0\sqrt{2\pi}} \exp\left(-\frac{(x-x_0)^2}{\sigma_0^2}\right), \tag{19}$$

$$n_{\mathrm{p}}(x,t=0) = n_{\mathrm{e}}(x,t=0), \quad n_{\mathrm{n}}(x,t=0) = 0. \tag{20}$$

Here N_{e0} is the initial number of electrons with Gaussian distribution centered at x_0 and standard deviation σ_0. The numerical scheme uses second-order central finite differences for discretization of spatial derivatives and classical fourth-order Runge–Kutta 4 scheme for integration in time. With such an explicit method there are at least two stability conditions for the time step [53]:

$$\Delta t < C_{\mathrm{a}}\,\Delta x\,/W \quad \text{(CFL condition)}, \tag{21}$$

$$\Delta t < C_{\mathrm{d}}\,(\Delta x)^2/D_{\mathrm{L}} \quad \text{(explicit diffusion limit)}, \tag{22}$$

where Δx is the spatial grid step. C_{a} and C_{d} are the maximum Courant numbers for advection and diffusion equations [54], which generally depend on the particular time integration scheme and spatial discretization. In our calculations, we use a small constant time step which meets the above criteria.

Finally, the induced current is calculated using Ramo's theorem [55]

$$i(t) = e_0\,\pi R_0^2\,\frac{E_{\mathrm{w}}}{V_{\mathrm{w}}}\int_0^d n_{\mathrm{e}}(x,t)\; W_{\mathrm{F}}(|E(x,t)|)\,\mathrm{sgn}(E(x,t))\,\mathrm{d}x, \tag{23}$$

where $E_{\mathrm{w}}/V_{\mathrm{w}}$ is the weighting field and W_{F} is the flux drift velocity [27].

3. Results and discussion

3.1. Preliminaries

The results for three RPC configurations considered in this section are obtained using the model described in section 2.3. Electron transport data required by this model are presented in section 2.2. Parameter values for the radius of cylindrical charge distribution R_0, photon mean free path λ and photoionization factor M, should generally require careful consideration. For example, the 'range' of the space charge field depends on R_0 which, on the other hand, is determined by the lateral spread of the primary ionization and transverse diffusion. Also, photoionization is a complex process, especially in the case of these RPC gas mixtures, and cannot be fully described by the effective parameters introduced in section 2.3. However, it is not the aim of this work to model the exact experimental conditions. The values for these parameters

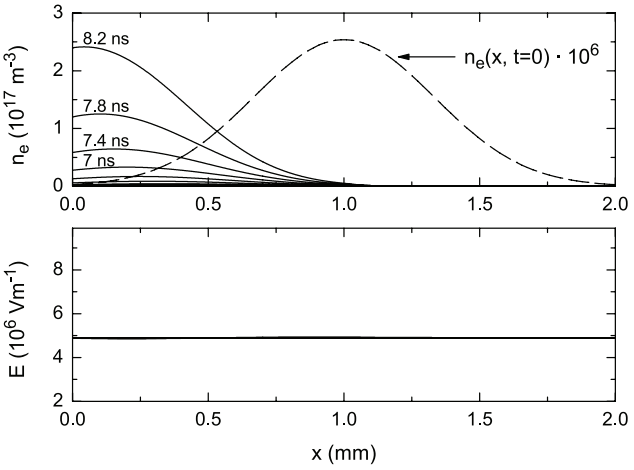

Figure 5. Electron number density and electric field during avalanche development in ATLAS triggering RPC (0–8.2 ns in steps of 0.4 ns). The applied electric field $E_0 = 4.9$ MV m^{-1} (196 Td) is oriented in the x direction.

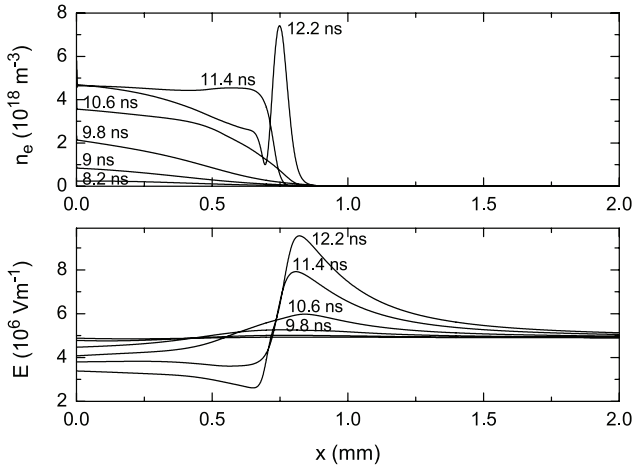

Figure 6. Electron number density and electric field during positive streamer formation in ATLAS triggering RPC (8.2–12.2 ns in steps of 0.8 ns). The applied electric field $E_0 = 4.9$ MV m^{-1} (196 Td) is oriented in the x direction.

are taken from [51], since they seem realistic: $R_0 = 0.3$ mm, $\lambda = 500$ μm and $M = 10^{-6}$.

Other parameters—gas gap length d, number of spatial cells m, initial number of electrons N_{e0}—are specific for each RPC configuration:

(i) ATLAS triggering RPC [3] with a gas mixture of 94.7% $C_2H_2F_4$ + 5% iso-C_4H_{10} + 0.3% SF_6 ($d = 2$ mm, $m = 3000$, $N_{e0} = 60$).
(ii) A single gas gap of the ALICE timing RPC [4] with a gas mixture of 90% $C_2H_2F_4$ + 5% iso-C_4H_{10} + 5% SF_6 ($d = 0.25$ mm, $m = 2000$, $N_{e0} = 6$).
(iii) Timing RPC [32] with a gas mixture of 85% $C_2H_2F_4$ + 5% iso-C_4H_{10} + 10% SF_6 ($d = 0.3$ mm, $m = 2000$, $N_{e0} = 9$).

Numbers for N_{e0} correspond to approximately 10 primary clusters mm^{-1} and 3 electrons/cluster, which are realistic average values. We assume that the initial electron distribution is a Gaussian (19) centred in the gas gap i.e. $x_0 = d/2$, with $\sigma_0 = d/6$. For simplicity, the weighting field is set to $E_w/V_w = 1/d$ as in the parallel plate chamber. We assume that the gas number density $N = 2.505 \cdot 10^{25}$ m^{-3}, which corresponds to the pressure of 1 atm and temperature of 293 K.

3.2. Electron avalanche and streamer development

We now consider the electron avalanche and streamer development in ATLAS triggering RPC. The applied electric field $E_0 = 4.9$ MV m^{-1} ($E_0/N = 196$ Td) is oriented along the x-axis and corresponds to the operating point voltage $U = 9.8$ kV [3]. Bulk transport data are employed in the model. The initial conditions assume 60 electrons with Gaussian distribution, as described in sections 2.3 and 3.1.

During the first 8.2 ns (figure 5), the electron avalanche exhibits typical exponential growth without noticeable space charge effects. Still, about half of the electrons have reached the anode. While electrons are being consumed at the anode the ions remain immobile. As a result, the space charge field

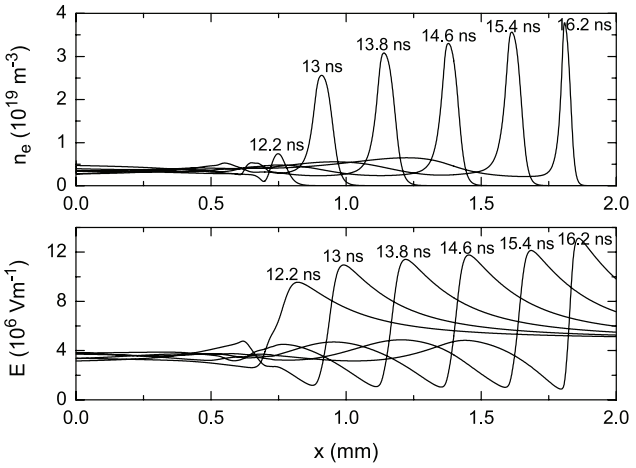

Figure 7. Electron number density and electric field during positive streamer propagation in ATLAS triggering RPC (12.2–16.2 ns in steps of 0.8 ns). The applied electric field $E_0 = 4.9$ MV m^{-1} (196 Td) is oriented in the x direction.

begins to grow and reaches 10% of the external field at about 10.6 ns (figure 6). Due to space charge, the external field is suppressed near the anode and enhanced at the tail of electron distribution. In this region of enhanced field a positive streamer is formed as a peak in the electron distribution (12.2 ns). At this moment, the space charge field reaches almost 100% of the external field, leading to high photon production. Due to photoionization, the positive streamer progresses toward the cathode (figure 7). After about 16.2 ns, the streamer peak becomes narrower and starts to diminish slowly.

The development of the electron avalanche and streamer is tightly related to the induced current, which is considered in the next section. It is interesting to note that in this case of ATLAS triggering RPC, but also in other RPC configurations considered in this work, the enhancement of the electric field which leads to the positive streamer formation is mainly due to electron absorption effect of the anode. A similar behavior was also observed in a parallel plate chamber [51].

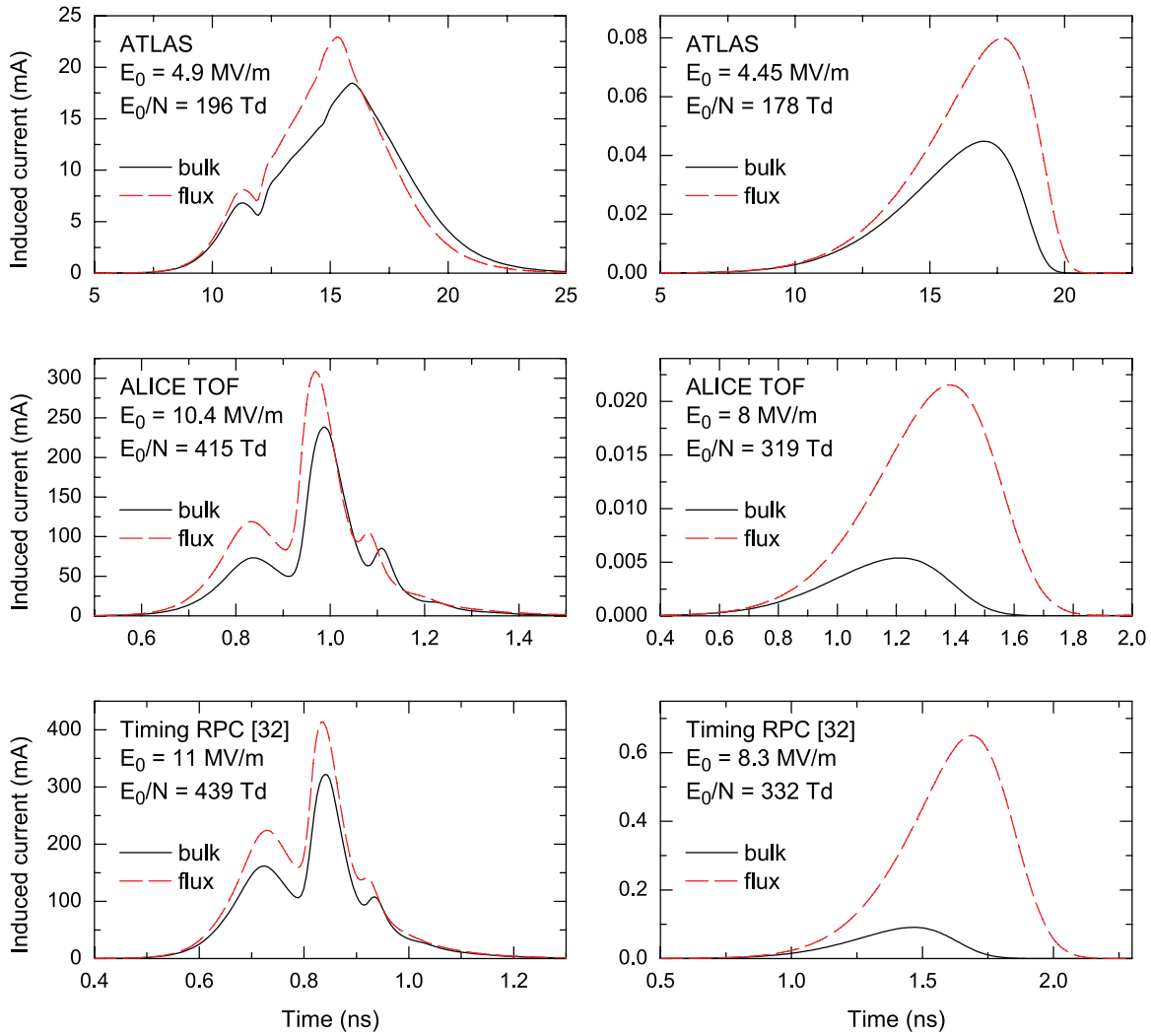

Figure 8. Induced signals in ATLAS triggering RPC, ALICE timing RPC (ALICE TOF) and timing RPC [32] calculated using flux and bulk transport data. Calculations are made for different applied electric fields E_0: realistic operating fields (left) and low operating fields leading to saturated avalanche without positive streamer formation (right).

3.3. Induced current

Figure 8 (top left, solid line) shows the induced current calculated for the case of ATLAS triggering RPC discussed in section 3.2. We observe a small precursor signal followed by a large peak. The occurrence of the precursor was also noticed in many experiments [56–58]. According to equation (23), the signal development can be interpreted knowing the electron number density and flux drift velocity. In our case, the flux drift velocity increases monotonically with the electric field strength (figure 2). We now recall the characteristic time intervals for the avalanche development (0–8.2 ns), streamer development (8.2–12.2 ns) and positive streamer propagation (12.2–16.2 ns) described by the electron number density and electric field strength in figures 5–7 respectively. During the avalanche phase, the induced current grows exponentially until the electrons reach the anode. Eventually, the exponential rise stops and becomes linear due to both electron absorption and space charge effects, which begin at about 10 ns. The induced current peaks at 11.3 ns and starts to drop off forming the characteristic precursor shape. Another rise begins when

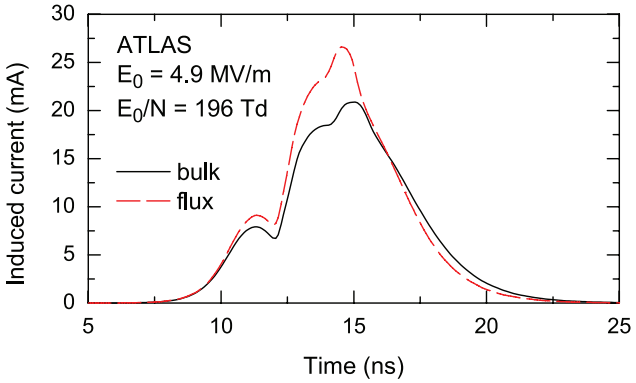

Figure 9. Induced signal in ATLAS triggering RPC calculated assuming the initial electron distribution with 10 equally spaced Gaussian clusters per mm, and 3 electrons per cluster. Calculations are made using flux and bulk transport data.

photoionization takes place in the region of enhanced electric field. The positive streamer is formed at 12.2 ns and the current rises while the positive streamer grows and propagates toward the cathode. At 16.2 ns the positive streamer stops

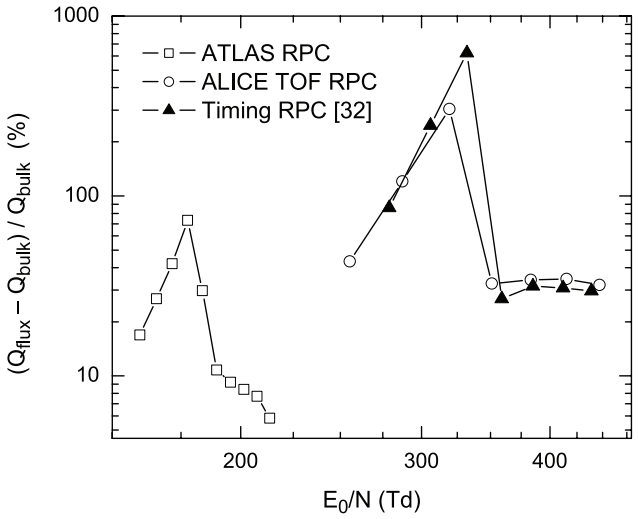

Figure 10. Percentage difference between the induced charges Q_{flux} and Q_{bulk}, calculated over a range of applied electric fields for ATLAS triggering RPC, ALICE timing RPC (ALICE TOF) and timing RPC [32].

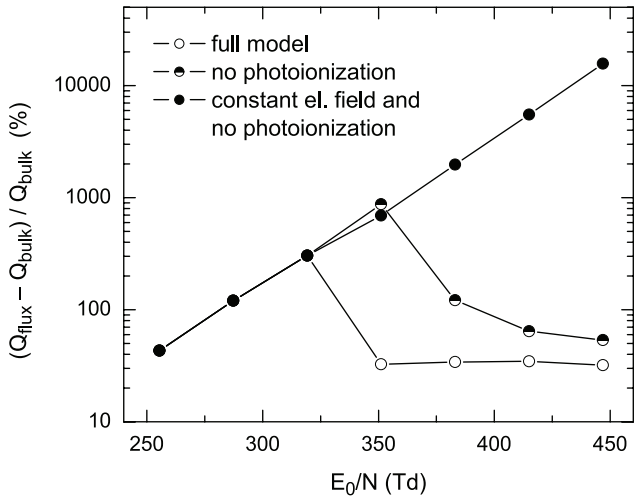

Figure 11. Percentage difference between the induced charges Q_{flux} and Q_{bulk} for the ALICE timing RPC. The difference is calculated over a range of applied electric fields for three modeling scenarios: (1) full model, (2) no photoionization, and (3) constant electric field and no photoionization.

right before reaching the cathode and starts to diminish, while the induced current slowly drops to zero.

The induced current for the ATLAS RPC calculated using flux transport data is also shown in figure 8 (top left, dashed line). In this case, the induced current is slightly larger than when bulk transport data are employed. Clearly, the difference between the two cases arises from the drift-diffusion equation (13) and not Ramo's theorem (23) where only flux drift velocity is used. This difference can be understood by considering a simple avalanche growth with multiplication factor $\exp((\nu_{\text{i}} - \nu_{\text{a}})l/W)$ where l is the distance to the anode. Indeed, since in RPC gases the bulk drift velocity is higher than flux drift velocity (figure 2), the avalanche multiplication factor will be higher in the flux case. The difference is even more pronounced at lower electric field of 178 Td where saturated avalanche does not progress into positive streamer (figure 8, top right).

In addition to single Gaussian initial conditions, we have also calculated the induced current in the case of ATLAS RPC with $E_0/N = 196$ Td, where the initial distribution consists of multiple Gaussians representing primary ionization with 10 clusters mm^{-1} and 3 electrons/cluster. The distribution is given as $n_{\text{e}}(x, t = 0) = \sum_{i=0}^{20} G(i \cdot 0.1 \text{ mm}, \sigma_0)$ where $G(x_0, \sigma_0)$ is a Gaussian defined in (19) with $N_{\text{e}0} = 3$ electrons and $\sigma_0 = 0.1$ mm/6. The results with this initial condition are shown in figure 9. Compared to the single Gaussian case, the induced current has a similar shape but with steeper rising edge and slightly rounded peak. These differences are mainly due to clusters near the cathode, which form a tail of the single Gaussian made by merging of small clusters during the avalanche and streamer formation phase.

Figure 8 shows the induced currents for ALICE timing RPC and timing RPC [32]. In contrast to ATLAS triggering RPC, the induced signals of timing RPCs at their operating fields are larger in amplitude, shorter in duration and rise faster as a consequence of higher electric fields and smaller gas gaps. For example, in case of ALICE timing RPC (figure 8, middle left), the peak due to positive streamer is smaller and has a faster rising edge than in case of ATLAS RPC. It is also followed by a small peculiar peak after about 0.1 ns. We have not fully investigated the origin of this small peak but it shows no sign of numerical artifact. Also, due to greater difference between flux and bulk transport data (figures 2 and 4) the difference between corresponding signals is larger compared to ATLAS RPC, especially at lower electric field (figure 8, middle right).

The results for the three RPC configurations and gas mixtures presented in this section show an interesting behavior—the discrepancy between the induced currents, calculated with flux and bulk transport data, decreases with the applied electric field strength. One should expect the opposite, knowing that the difference between the flux and bulk transport data increases with the electric field in RPC operating range (figures 2 and 4). This phenomenon is discussed in the following section.

3.4. Induced charge

In this section, we investigate the impact of electron transport data on the fast component of the induced charge. The induced charge is calculated as an integral of the induced current i.e. $Q = \int_0^{+\infty} \text{i}(t)\,\text{d}t$. Figure 10 shows the percentage difference between the induced charges Q_{flux} and Q_{bulk}, obtained using flux and bulk transport data, respectively. The difference is calculated over a range of operating electric fields for the three RPC configurations. The difference ranges from 6% for the ATLAS RPC up to 600% for the timing RPC [32]. This is understandable considering the corresponding transport data. However, for each of these RPC configurations, the difference grows with the electric field up to a certain point when it drops abruptly. We note that the induced currents on the left side of the figure 8 are calculated using the applied fields above this threshold, while figures on the right side are calculated using applied fields below the threshold. This behavior seems

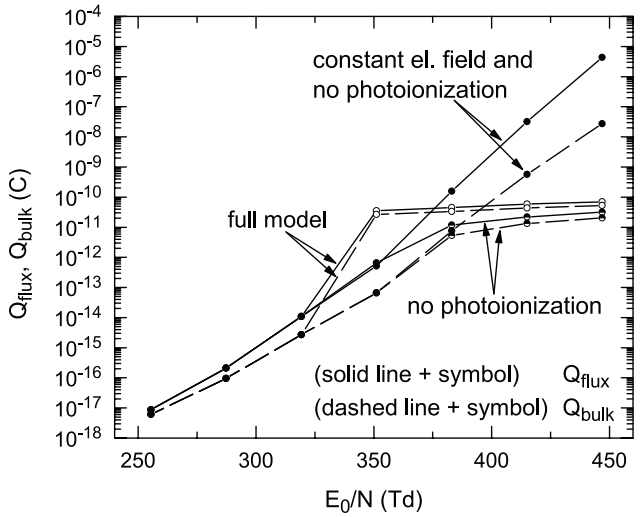

Figure 12. Induced charges Q_{flux} and Q_{bulk} calculated over a range of applied electric fields for the ALICE timing RPC using three modeling scenarios: (1) full model, (2) no photoionization and (3) constant electric field and no photoionization.

counter-intuitive considering that above ∼100 Td the difference between flux and bulk transport data grows monotonically with the electric field. Moreover, the space charge effects can increase this difference even further through enhancement or reduction of the electric field toward the regions where flux and bulk transport data differ considerably (figures 2 and 4).

In order to investigate this effect, we modify our model from section 2.3 to include two more scenarios: (1) no photoionization ($S_{\text{ph}}(x,t) \equiv 0$), and (2) constant electric field i.e. no space charge effects, and no photoionization ($E(x,t) \equiv E_0$, $S_{\text{ph}}(x,t) \equiv 0$). These two scenarios in addition to the full model are used to calculate the percentage difference between the induced charges Q_{flux} and Q_{bulk} for the ALICE timing RPC (figure 11). It is evident that without space charge effects and photoionization the difference grows steadily with the electric field. Without photoionization, the space charge effects slightly enhance the difference at 351 Td. Above this electric field, the difference decreases continuously due to space charge effects alone. The photoionization only suppresses the difference more rapidly since it produces additional space charge.

Figure 12 shows the induced charges Q_{flux} and Q_{bulk} for the ALICE timing RPC calculated using the three modeling scenarios. The saturation effect induced by the space sharge is clearly visible. Since $Q_{\text{flux}} > Q_{\text{bulk}}$, more space charge is produced in the flux case. Therefore, Q_{flux} saturates faster with the electric field than Q_{bulk} and the difference between them starts to drop. The inclusion of photoionization results in more space charge and consequently faster saturation. It is also seen that, in an isolated case of Q_{flux} at 351 Td, the space charge effects can slightly increase the induced charge. We should also note that the calculated induced charge seems unrealistically large compared to some experimental data for the fast component of the induced charge [32, 58]. This can be due to many reasons including the constraints of the 1.5D model itself, but also its parameters which are not determined accurately such as radius R_0 and photoionization parameters δ, λ and Q. Still, the most obvious factor is the weighting field E_w/V_w which we assume as $1/d$. Depending on the electrode permittivity and thickness, the weighting field for some RPC geometries can be a few times smaller than $1/d$.

4. Conclusion

In this work we have discussed some aspects of electron transport in gases relevant for modeling of RPCs. Under hydrodynamic conditions, we have shown how the difference between flux and bulk transport data arises due to presence of non-conservative collisions. The duality of transport data was clearly visible in case of three RPC gas mixtures with different SF_6 content. One important implication is that in modeling of electron avalanches, bulk data should generally be used. A fluid model with photoionization was developed in order to demonstrate how the transport data used as input affect the results of RPC modeling. Using this model we have investigated the streamer development in ATLAS triggering RPC. It was found that the electron absorption on the anode has large influence on the space charge effects and positive streamer formation. The model was also used to calculate the induced signals for ATLAS triggering RPC, ALICE timing RPC and timing RPC [32]. The most striking observation is the difference between the induced charges calculated using flux and bulk data. This difference can reach up to 80% in case of ATLAS RPC or several hundred percent in case of timing RPCs at lower operating fields. However, at higher electric fields the saturation effect due to space charge and photoionization lowers the difference to about 6% for the ATLAS RPC and 30% for the timing RPCs. This illustrates the importance of correct implementation of data in modeling. One should be aware of the origin of the transport data and the type of transport data required in modeling.

The formalism and methodology presented in this paper are valid for other types of gaseous particle detectors. Many of the methods and techniques developed in the framework of swarm physics directly carry over to the particle detectors. We are currently working on extending the fluid treatment of RPCs to include more balance equations and utilizing momentum transfer theory [25] to evaluate the collisional terms. This will facilitate a full fluid treatment of RPCs using state-of-the-art theory.

Acknowledgments

This work was supported by MPNTRRS Projects OI171037 and III41011.

References

[1] Santonico R and Cardarelli R 1981 *Nucl. Instrum. Methods* **187** 377–80
[2] Cardarelli R, Santonico R, Di Biagio A and Lucci A 1988 *Nucl. Instrum. Methods* A **263** 20–5
[3] The ATLAS Collaboration 2008 *J. Instrum.* **3** S08003
[4] The ALICE Collaboration 2008 *J. Instrum.* **3** S08002
[5] The CMS Collaboration 2008 *J. Instrum.* **3** S08004

[6] Santonico R 2012 *Nucl. Instrum. Methods* A **661** S2–5
[7] Fonte P 2002 *IEEE Trans. Nucl. Sci.* **49** 881–7
[8] Iuppa R 2015 *J. Instrum.* **10** C04044
[9] Cârloganu C *et al* 2013 *Geosci. Instrum. Methods Data Syst.* **2** 55–60
[10] Couceiro M, Crespo P, Mendes L, Ferreira N, Ferreira Marques R and Fonte P 2012 *Nucl. Instrum. Methods* A **661** S156–8
[11] Mangiarotti A, Fonte P and Gobbi A 2004 *Nucl. Instrum. Methods* A **533** 16–21
[12] Riegler W 2009 *Nucl. Instrum. Methods* A **602** 377–90
[13] Riegler W and Lippmann C 2004 *Nucl. Instrum. Methods* A **518** 86–90
[14] Salim M, Hasan R, Majumdar N, Mukhopadhayay S and Satyanarayana B 2012 *J. Instrum.* **7** P11019
[15] Bošnjaković D, Petrović Z Lj and Dujko S 2014 *J. Instrum.* **9** P09012
[16] Khosravi Khorashad L, Moshaii A and Hosseini S 2011 *Europhys. Lett.* **96** 45002
[17] Moshaii A, Khosravi Khorashad L, Eskandari M and Hosseini S 2012 *Nucl. Instrum. Methods* A **661** S168–71
[18] Fonte P 2013 *J. Instrum.* **8** P11001
[19] Petrović Z Lj, Dujko S, Marić D, Malović G, Nikitović Ž, Šašić O, Jovanović J, Stojanović V and Radmilović-Raenović M 2009 *J. Phys. D: Appl. Phys.* **42** 194002
[20] Petrović Z Lj, Šuvakov M, Nikitović Ž, Dujko S, Šašić O, Jovanović J, Malović G and Stojanović V 2007 *Plasma Sources Sci. Technol.* **16** S1–12
[21] Dujko S, White R D and Petrović Z Lj 2008 *J. Phys. D: Appl. Phys.* **41** 245205
[22] Dujko S, White R D, Raspopović Z M and Petrović Z Lj 2012 *Nucl. Instrum. Methods* B **279** 84–91
[23] White R D, Dujko S, Ness K F, Robson R E, Raspopović Z and Petrović Z Lj 2008 *J. Phys. D: Appl. Phys.* **41** 025206
[24] Dujko S, White R D, Petrović Z Lj and Robson R E 2010 *Phys. Rev.* E **81** 046403
[25] White R D, Robson R E, Dujko S, Nicoletopoulos P and Li B 2009 *J. Phys. D: Appl. Phys.* **42** 194001
[26] Biagi S F 1999 *Nucl. Instrum. Methods* A **421** 234–40
[27] Robson R E 1991 *Aust. J. Phys.* **44** 685
[28] Sakai Y, Tagashira H and Sakamoto S 1977 *J. Phys. D: Appl. Phys.* **10** 1035–49
[29] BOLSIG + www.bolsig.laplace.univ-tlse.fr version: 07/2015
[30] Dujko S, Raspopović Z M, Petrović Z Lj and Makabe T 2003 *IEEE Trans. Plasma Sci.* **31** 711–6
[31] Bošnjaković D, Petrović Z Lj, White R D and Dujko S 2014 *J. Phys. D: Appl. Phys.* **47** 435203
[32] Lopes L, Fonte P and Mangiarotti A 2012 *Nucl. Instrum. Methods* A **661** S194–7
[33] Kumar K, Skullerud H R and Robson R E 1980 *Aust. J. Phys.* **33** 343
[34] Dujko S, White R D, Ness K F, Petrović Z Lj and Robson R E 2006 *J. Phys. D: Appl. Phys.* **39** 4788–98
[35] Ness K F and Robson R E 1986 *Phys. Rev.* A **34** 2185–209
[36] Nolan A M, Brennan M J, Ness K F and Wedding A B 1997 *J. Phys. D: Appl. Phys.* **30** 2865–71
[37] Legler W 1961 *Z. Naturforsch.* **16a** 253
[38] Riegler W, Lippmann C and Veenhof R 2003 *Nucl. Instrum. Methods* A **500** 144–62
[39] Basile G, Gallimberti I, Stangherlin S and Teich T H 1991 Swarm parameters for tetrafluorethane (HFA 134a) *Proc. XX Int. Conf. on Phenomena in Ionized Gases* vol 2, ed M Vaselli p 361
[40] de Urquijo J, Juárez A M, Basurto E and Hernández-Ávila J L 2009 *Eur. Phys. J.* D **51** 241–6
[41] Dujko S, Markosyan A H, White R D and Ebert U 2013 *J. Phys. D: Appl. Phys.* **46** 475202
[42] Markosyan A H, Teunissen J, Dujko S and Ebert U 2015 *Plasma Sources Sci. Technol.* **24** 065002
[43] Dujko S, Raspopović Z M and Petrović Z Lj 2005 *J. Phys. D: Appl. Phys.* **38** 2952–66
[44] Šašić O *et al* 2016 *Eur. Phys. J.* D to be submitted
[45] Šašić O, Dupljanin S, de Urquijo J and Petrović Z Lj 2013 *J. Phys. D: Appl. Phys.* **46** 325201
[46] Lima I B, Mangiarotti A, Vivaldini T C, Gonçalves J A C, Botelho S, Fonte P, Takahashi J, Tarelho L V and Bueno C C 2012 *Nucl. Instrum. Methods* A **670** 55–60
[47] Itoh H, Matsumura T, Satoh K, Date H, Nakao Y and Tagashira H 1993 *J. Phys. D: Appl. Phys.* **26** 1975–9
[48] Petrović Z Lj, Crompton R W and Haddad G N 1984 *Aust. J. Phys.* **37** 23
[49] Robson R E 1984 *Aust. J. Phys.* **37** 35
[50] Davies A J, Evans C J and Jones F L 1964 *Proc. R. Soc.* A **281** 164–83
[51] Fonte P 1996 *IEEE Trans. Nucl. Sci.* **43** 2135–40
[52] Kline L E 1974 *J. Appl. Phys.* **45** 2046
[53] Hundsdorfer W and Verwer J 2003 *Numerical Solution of Time-Dependent Advection-Diffusion-Reaction Equations* (*Springer Series in Computational Mathematics* vol 33) (Berlin: Springer)
[54] Courant R, Friedrichs K and Lewy H 1928 *Math. Ann.* **100** 32–74
[55] Ramo S 1939 *Proc. IRE* **27** 584
[56] Anderson D F, Kwan S and Peskov V 1994 *Nucl. Instrum. Methods* A **348** 324–8
[57] Cardarelli R, Makeev V and Santonico R 1996 *Nucl. Instrum. Methods* A **382** 470–4
[58] Fonte P, Smirnitski A and Williams M C S 2000 *Nucl. Instrum. Methods* A **443** 201–4